INTERACTION OF CORRODING IRON WITH BENTONITE IN THE ABM1 EXPERIMENT AT ÄSPÖ, SWEDEN: A MICROSCOPIC APPROACH

Paul Wersin*, Andreas Jenni, and Urs K. Mäder

Institute of Geological Sciences, University of Bern, Baltzerstrasse 1+3, 3012 Bern, Switzerland

Abstract—Bentonite and iron metals are common materials proposed for use in deep-seated geological repositories for radioactive waste. The inevitable corrosion of iron leads to interaction processes with the clay which may affect the sealing properties of the bentonite backfill. The objective of the present study was to improve our understanding of this process by studying the interface between iron and compacted bentonite in a geological repository-type setting. Samples of MX-80 bentonite samples which had been exposed to an iron source and elevated temperatures (up to 115ºC) for 2.5 y in an *in situ* experiment (termed ABM1) at the Äspö Hard Rock Laboratory, Sweden, were investigated by microscopic means, including scanning electron microscopy, μ-Raman spectroscopy, spatially resolved X-ray diffraction, and X-ray fluorescence.

The corrosion process led to the formation of a ~100 μm thick corrosion layer containing siderite, magnetite, some goethite, and lepidocrocite mixed with the montmorillonitic clay. Most of the corroded Fe occurred within a 10 mm-thick clay layer adjacent to the corrosion layer. An average corrosion depth of the steel of 22−35 μm and an average Fe^{2+} diffusivity of $1-2 \times 10^{-13}$ m^2/s were estimated based on the properties of the Fe-enriched clay layer. In that layer, the corrosion-derived Fe occurred predominantly in the clay matrix. The nature of this Fe could not be identified. No indications of clay transformation or newly formed clay phases were found. A slight enrichment of Mg close to the Fe−clay contact was observed. The formation of anhydrite and gypsum, and the dissolution of some SiO_2 resulting from the temperature gradient in the *in situ* test, were also identified.

Key Words—Bentonite, Iron, *In Situ* Experiment, Interface.

INTRODUCTION

Bentonites are used for a variety of engineering and household applications (Carrado and Komadel, 2009; Christidis and Huff, 2009; Eisenhour and Brown, 2009; Gates *et al.*, 2009; Güven, 2009; Williams *et al.*, 2009). For example, compacted bentonite is envisaged as a backfill material in many geological-repository concepts for radioactive waste because of its favorable properties such as swelling capacity, plasticity, nanoporous structure, and retention capacity for radionuclides (*e.g.* NAGRA, 2002; SKB, 2011; Posiva, 2013). These properties may be compromised in geological-repository environments by interaction of the bentonite with reactive components such as cementitious or metallic materials. For example, in the Swiss high-level nuclear waste disposal concept, waste-containing steel canisters and compacted bentonite will be placed in horizontal deposition tunnels. Upon closure of the repository, the bentonite will be saturated by the ingress of natural porewater from the surrounding host rock. Concomitantly, the bentonite clay will experience elevated temperatures (up to ~130ºC) originating from the radioactive decay of the waste. During saturation, canister corrosion will be initiated, first under aerobic

conditions, which will rapidly turn anaerobic by reaction of oxygen with the steel canister and with Fe-bearing minerals (*e.g.* pyrite) in the bentonite (Wersin *et al.*, 2004). From thermo-hydraulic calculations the saturation process is estimated to last for a period of decades up to a few hundreds of years (NAGRA, 2002). The anaerobic corrosion process, however, will last much longer ($>10^5$ y) and release dissolved mobile iron species which will react with the clay (Bradbury *et al.*, 2014). Details of the interaction of iron species released by corrosion and the clay are still not well understood. Several related processes affecting the barrier function of the bentonite backfill have been recognized, including: (1) local cementation of the bentonite by precipitation of Fe(II)/(III) oxides and hydroxides (Carlson *et al.*, 2007); (2) destabilization of the dioctahedral smectite structure (Lantenois *et al.*, 2005); (3) transformation of the montmorillonite to a non-swelling iron phyllosilicate, such as berthierine (Mosser-Ruck *et al.*, 2010); (4) dissolution of the montmorillonite during pH increase due to the iron-corrosion process (Marty *et al.*, 2010; Wersin and Birgersson, 2014); or even (5) direct interaction of H_2 with structural Fe in the smectite (Didier *et al.*, 2012).

A number of recent studies have looked at the effects of corroding iron on alteration in bentonite and in other clay materials; reviews of this topic include those by Wersin *et al.* (2007) and Bradbury *et al.* (2014). Most studies have examined idealized laboratory systems,

* E-mail address of corresponding author:
paul.wersin@geo.unibe.ch

tuned to enhance the effect of Fe−clay interaction. Smectite transformation to 1:1 phyllosilicates such as berthierine, cronstedtite, and odinite together with iron (oxyhydr)oxides has been observed in batch experiments at conditions of high liquid/solid ratios, high Fe/clay ratios, and low to moderate temperatures (20−90ºC) (Lantenois *et al.*, 2005; Perronnet *et al.*, 2008; Osacky *et al.*, 2010; Kumpulainen *et al.*, 2010; De Combarieu *et al.*, 2011; Lanson *et al.*, 2012; Jodin-Caumon *et al.*, 2010, 2012). At higher temperatures (100−300ºC), Fe-rich smectite (dioctahdral and trioctahedral) and/or chlorite minerals were identified (Guillaume *et al.*, 2003, 2004; Wilson *et al.*, 2006; Charpentier *et al.*, 2006; Mosser-Ruck *et al.*, 2010; Jodin-Caumon *et al.*, 2010, 2012), sometimes associated with newly formed zeolites (Wilson *et al.*, 2006; Charpentier *et al.*, 2006). Comparatively few studies have examined more realistic repository settings, *i.e.* low liquid/solid and Fe/clay ratios. Generally speaking, much less smectite alteration has been noted under such conditions, but magnetite (Papillon *et al.*, 2001; Carlson *et al.*, 2007; Martin *et al.*, 2008; Gaudin *et al.*, 2009), iron oxyhydroxides (Carlson *et al.*, 2007; Gaudin *et al.*, 2009), and siderite (Papillon *et al.*; 2001; Schlegel *et al.*, 2010) were observed as corrosion products. The experimental study of Martin *et al.* (2008) tested the corrosion behavior of iron in contact with compacted MX-80 bentonite and with a clayrock (Callovo-Oxfordian formation, Bure, France). In both cases, corrosion layers of magnetite and siderite were found, whereas only in the case of the clayrock was an intermediate Fe-, O-, Na-, and Si-containing layer (tentatively interpreted as consisting of phyllosilicates) observed. Later, the same research group (Schlegel *et al.*, 2010; 2014) identified the formation of a layer of Fe-rich 7 Å phyllosilicates in addition to chukanovite ($Fe_2CO_3(OH)_2$), magnetite, and siderite for Callovo-Oxfordian clayrock block samples exposed to an anaerobically corroding iron source.

In spite of the numerous investigations, understanding of the process of Fe−clay interaction remains rather sketchy, especially with respect to long-term behavior. Thus, uncertainties in predicting the stability of the bentonite backfill in contact with reactive metal iron components persist. In particular, this uncertainty is related to the mineralogical and hydraulic properties of the contact area between the iron and the clay (Johnson *et al.*, 2008).

The present study focuses on the contact area between a corroding iron source and compacted MX-80 bentonite that had been emplaced as highly compacted pellets in the ABM1 (Alternative Buffer Materials) *in situ* experiment at the Äspö Hard Rock Laboratory (Sweden) which was designed to simulate repository-like conditions. The objective is to obtain quantitative and qualitative process understanding of corrosion and Fe−bentonite interaction in a realistic repository setting with variable redox conditions and temperatures of ~100ºC. A secondary objective was to develop and optimize analytical methods to characterize the Fe−clay contact area which should be applied later to the samples from further ongoing, long-term *in situ* tests.

Two recent studies have analyzed different bentonite samples and the contact with the metal heater in the ABM1 test. Kaufhold *et al.* (2013) studied different pre-compacted bentonite block materials with standard techniques including X-ray diffraction (XRD), X-ray fluorescence (XRF), and Fourier-transform infrared (FTIR) spectroscopy, and focused on potential alterations in the bentonite materials. Some changes close to the contact with the steel were observed, including the accumulation of anhydrite and organic carbon and the dissolution of cristobalite in some samples, a general increase in iron, and the presence of siderite in one sample. In the second study, by Svensson and Hansen (2013), several bentonite materials, precompacted as blocks, from the ABM1 test and another *in situ* test were studied with XRD and X-ray absorption near edge structure spectroscopy (XANES) in terms of potential alterations and Fe(II)/Fe(III) distributions in the clay. The authors found that the Fe(II)/Fe(III) ratio had increased towards the steel heater, but otherwise only small changes had occurred, such as minor dissolution of cristabolite, an increase in the Mg content and a small shift in the 060 peak, indicative of trioctahedral smectite. The work presented here complements these studies, by looking at a specific type of granular compacted bentonite developed for backfilling in the Swiss repository concept (NAGRA, 2009). In contrast to the two other 'bulk-type' studies, the intact Fe interface was analyzed at a high spatial resolution with a microscopic approach including scanning electron microscopy-element dispersive spectroscopy (SEM/EDX) and spatially resolved μ-Raman spectroscopy. This enabled the authors to obtain quantitative information on the iron transfer from the corroding source to the clay.

EXPERIMENTAL AND ANALYTICAL METHODS

Characterization of the granular compacted bentonite material emplaced

The raw MX-80 bentonite with a mesh size of 16−200 (74−1000 μm) was purchased from the American Colloid Company (Sibelco Nordic Minerals, Cheshire, UK). The starting MX-80 and other bentonite materials in ABM1 were analyzed thoroughly with respect to their petrophysical, chemical, and mineralogical characteristics (Svensson *et al.*, 2011; NAGRA, 2011). The raw MX-80 was found to contain 80.5 ± 3.6 wt.% smectite, 6.0 ± 0.3 wt.% quartz, 0.6 ± 0.1 wt.% pyrite, 8.7 ± 0.6 wt.% feldspar, 2.6 ± 0.7 wt.% illite/muscovite, and 1.6 ± 0.7 wt.% calcite, as determined from quantitative XRD (Rietveld) analysis (NAGRA,

2011). In addition to those minerals, cristobalite and dolomite were identified from powder XRD data using a synchrotron X-ray source (Svensson *et al.*, 2011). The cation exchange capacity (CEC) was determined by the Cu(II)-triethylenetetramine method (Meier and Kahr, 1999) to be 80.2 ± 4.0 meq/100 g (Svensson *et al.*, 2011). The chemical composition determined by XRF (Svensson *et al.*, 2011) is presented in the Results section below. The MX-80 bentonites from the same supplier were analyzed previously by Karnland *et al.* (2006) and yielded similar results. Using a Leco multiphase carbon analyzer, those authors also found the organic carbon content to be ~0.2−0.3 wt.%. The granular bentonite material, which was emplaced in the ABM1 borehole (see below), consisted of highly compacted MX-80 pellets with a very low moisture

content (<5 wt.%) and a bimodal size distribution (Wollenberg and Schröder, 2006). The sealing properties and homogenization behavior during saturation under different temperature conditions had been studied previously using laboratory-scale samples (Karnland *et al.*, 2008).

The ABM1 test package, excavation, and on-site sampling

The ABM test is an internationally supported *in situ* experiment conducted by SKB (the Swedish Nuclear Fuel and Waste Management Co) in the Äspö Hard Rock Laboratory, Sweden. The main objective of ABM is to test the stability of different bentonites and other clay materials under adverse conditions, representative of the near-field of high-level radioactive waste repositories (Svensson *et al.*, 2011). Within the ABM test, three test
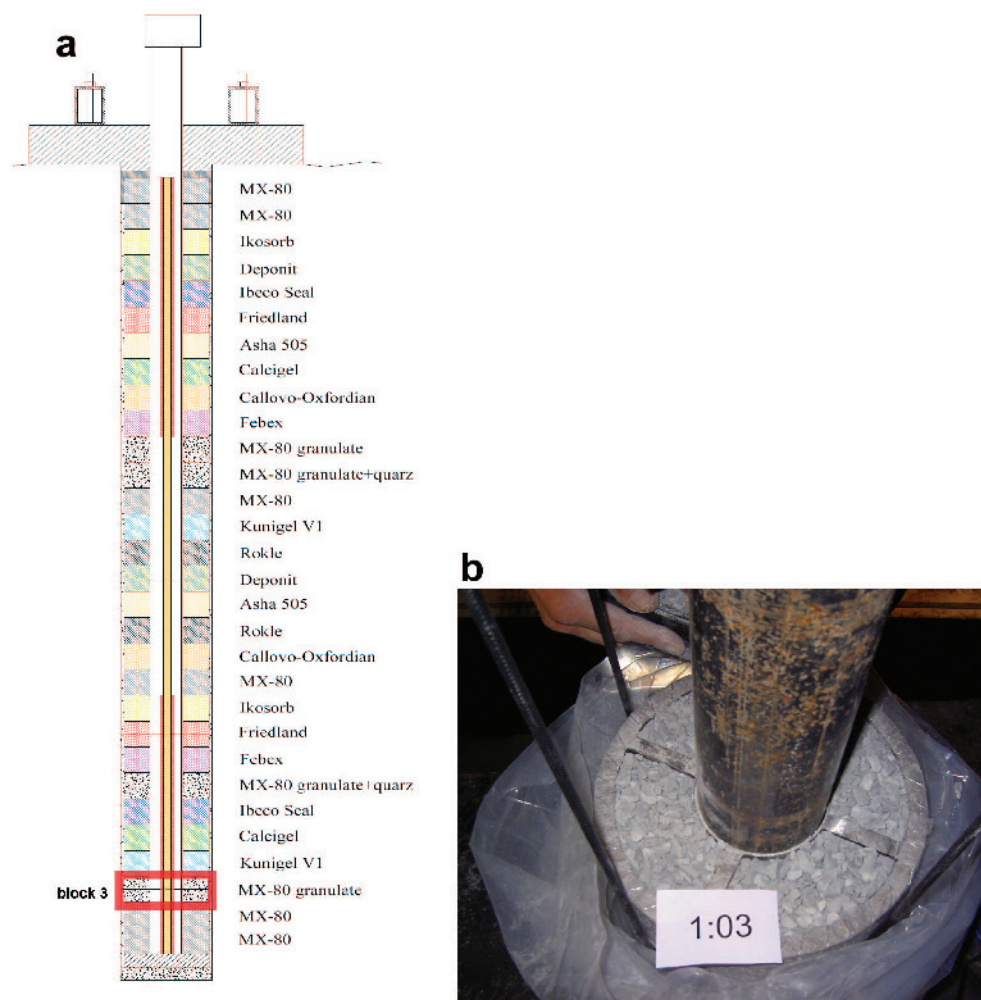

Figure 1. (a) Test layout of ABM1 showing the different clay materials stacked as blocks, each with a height of 100 mm in the borehole (diameter 300 mm). The total height of the stack is 3 m. In the center of the borehole is a steel tube which contains an electrical heating system. The position of block 3 marked in red. (b) Image of the pellet cage (block 3) during installation. The inner part of the cage is a metal ring (outer diameter = 108 mm); the outer cage is made of horizontal steel rings (outer diameter = 124 mm) and a steel fiber cloth. Steel bars on the top and the bottom of the cage reinforce its strength. The granular bentonite texture is clearly visible.

packages (ABM1, ABM2, and ABM3), consisting of various bentonite and other clay materials stacked upon each other as blocks, were placed in three boreholes and heated through a central steel tube (Figure 1a). The granular material of interest in this work was inserted in a prefabricated iron-based cage (Figure 1b) and emplaced as block 3. This circular cage was made of an inner cylindrical steel ring, steel frames, and fiber cloth wrapped around the cages (Figure 1b). The installation procedure was detailed by Eng *et al.* (2007). Descriptions of the experiment and its dismantling were presented by Svensson *et al.* (2011). Briefly, heating and wetting with artificial Äspö groundwater of the ABM1 test commenced on December 7, 2006. The bentonite materials were heated slowly and maximum temperatures were reached after ~1 y. Because of technical problems with the wetting system some variation in maximum temperatures occurred. The maximum heat output was generated for ~400 days as indicated by the temperature-monitoring data (Eng *et al.*, 2007). Block 3 was exposed to maximum temperatures of ~115ºC closest to the central tube and to ~75ºC close to the rock contact. The moisture content was not monitored during the test, but was analyzed after overcoring (see the Results section); consequently, the saturation history is unknown.

The experiment was overcored after 881 days on May 5, 2009, 18 days after shutdown of the heating system. Subsequently, it was lifted up in one piece and sawn into segments which were placed in plasticized aluminum bags, evacuated, and welded. Then the bags were placed in air-tight barrels and transported to the laboratory at Clay Technology (Lund, Sweden) for detailed sampling. Sub-sampling was performed with a band saw (for bentonite and some steel bars of cages) and a mechanical hack saw (for the central steel tube and

the bars of steel cages). Exposure to ambient air was minimized by covering surfaces with plastic foil and working swiftly. Cut-off sub-samples were immediately sealed in plasticized aluminum foil. Sharp edges of the steel cage (where present) were taped to protect the aluminum foil. Samples including iron components from the cage (inner cylinder, lateral bars, vertical bar) in block 3 were taken. Visual inspection of the granular bentonite material indicated no macroscopically discernible granular texture after the experiment.

The samples were transported to the University of Bern (Switzerland) and stored cool (~4ºC).

Petrophysical measurements

A sample of block 3 was cut with a band saw perpendicular to the borehole axis to prepare three subsamples: top, mid-height, and bottom of the block, each having a height of ~30 mm. From these, slices along radial profiles were cut for wet-density and water-content determinations along radial profiles for block 3. Higher-resolution 6-point radial profiles (radial length 15 mm) were determined at mid-height, and lower-resolution 3-point radial profiles (radial length 30 mm) were determined in parallel near the top and base (Table 1).

The water content (WC) was determined by heating the clay samples to 105ºC in a drying oven to constant weight (~48 h). The water content was calculated relative to the dry mass obtained at 105ºC. The error is estimated to be within 2%.

The wet density (ρ_{wet}) was measured in duplicate using the paraffin oil-displacement method. The error is estimated to be $<\pm5\%$. The dry density (ρ_{dry}) was calculated from the WC and the ρ_{wet}. The porosity was calculated from the dry density and a grain density of 2.754 g/cm^3 (Table 1).

Table 1. Petrophysical data of block 3 after the *in situ* test.

	Radial distance from cage ring (cm)	Water content dry (wt.%)	Wet density (g/cm^3)	Dry density (g/cm^3)	Porosity* (vol.%)	Degree of saturation
Half-height	0−1.5	33.85	1.93	1.44	47.5	1.03
	1.5−3	35.49	1.90	1.40	49.2	1.01
	3−4.5	35.94	1.89	1.39	49.5	1.01
	4.5−6	36.23	1.88	1.38	49.8	1.00
	6−7.5	37.50	1.88	1.37	50.3	1.02
	7.5−9.2	38.43	1.87	1.35	51.0	1.02
Near the top	0−3	35.33	1.91	1.41	48.9	1.02
	3−6	37.32	1.87	1.36	50.4	1.01
	6−9	40.27	1.84	1.31	52.4	1.01
Near the base	0−3	33.48	1.93	1.45	47.4	1.02
	3−6	34.56	1.90	1.41	48.8	1.00
	6−9	37.44	1.89	1.37	50.1	1.03

* calc. assuming a grain density of 2.754 g/cm^3 (NAGRA, 2011).

Analysis of Fe−clay contact zone

Sample preparation. Using a band saw, the packaged sample was cut in half perpendicular to the cylindrical steel ring axis of the cage (Figure 2a). Inspection of the freshly exposed surfaces confirmed that the original granular texture had disappeared during the saturation and heating process. A subsample for microscopic analysis was extracted (Figure 2b), packed in plastic foil under slight vacuum, and inserted into liquid nitrogen for ~30 min. During this procedure a crack developed between the bentonite and the metal. Subsequently, the sample was freeze dried using a Leybold-Heraeus GT 2 instrument (Leybold-Heraeus, Hanau, Germany) at a vacuum of 0.1 Torr for 4 h. The sample, bentonite and metal, was removed from the apparatus and embedded immediately in epoxy resin under vacuum. About 1 week later, a polished section across the steel−clay interface was prepared without water contact. The surface was processed using grinding paper, oil-based diamond suspensions, and petroleum. The resulting polished section was subsequently stored in a desiccator until further microscopic analysis.

A further subsample was prepared for XRF and XRD analysis (see section below). For this purpose, ~2−3 mm-thick slices of the moist material were cut with a plastic cutting tool parallel to the metal contact. After each slicing step, aliquots were prepared quickly for XRD analysis (see section below) and the remaining sample block was repackaged under vacuum in plastic foil to minimize drying and oxidation. For XRF, aliquots were also prepared after each slicing step.

XRD analyses. The small amount of powder made it impossible to carry out a standard clay preparation (Atterberg separation, glycol treatment, drying, *etc*.).

Instead, an aliquot of the moist clay material obtained from slicing of the clay sample (see above) was mounted quickly on a sample holder (front-loaded), the surface flattened with a glass slide, and inserted in a PANalytical X'Pert PRO X-ray diffractometer (PANalytical, Almelo, Netherlands). The samples were examined using CuKα radiation with a wavelength of 1.54 Å at 40 mA and 40 kV, and were scanned from 4 to 80º2θ using a step size of 0.0167º2θ and 10 s per step.

XRF analyses. Another aliquot of the moist clay material was dried to 105ºC in a drying oven for ~2 days. The dried samples were subsequently ground using a small tungsten carbide mill. Glass pellets were made by fusing a 1:10 mixture of sample powder and Li-tetraborate at 1100ºC. The XRF analyses of major elements were performed on a Philips PW 2400 spectrometer (Philips, Eindhoven, Netherlands) at the Department of Geosciences of the University of Fribourg, (Switzerland) and corrected with the internal Philips software *X40* on the basis of a set of international rock standards. Loss on ignition (LOI) was determined by mass difference before and after fusing.

SEM/EDX analyses. The uncoated sample surface was examined in a SEM (Zeiss EVO-50 XVP, Carl Zeiss Microscopy GmbH, Jena, Germany) equipped with an EDAX Sapphire light element detector in low-vacuum mode (10 Pa) with a beam acceleration of 20 kV, a sample current of 500 pA, and a working distance of 8.6 mm. The beam current was adjusted to yield a dead time of 20−30% for EDX analysis (energy dispersive spectroscopy). The EDX element maps with a resolution of 512×400 pixels were acquired using a dwell time of 200 μs/pixel, and frames were averaged for 8−12 h. Higher
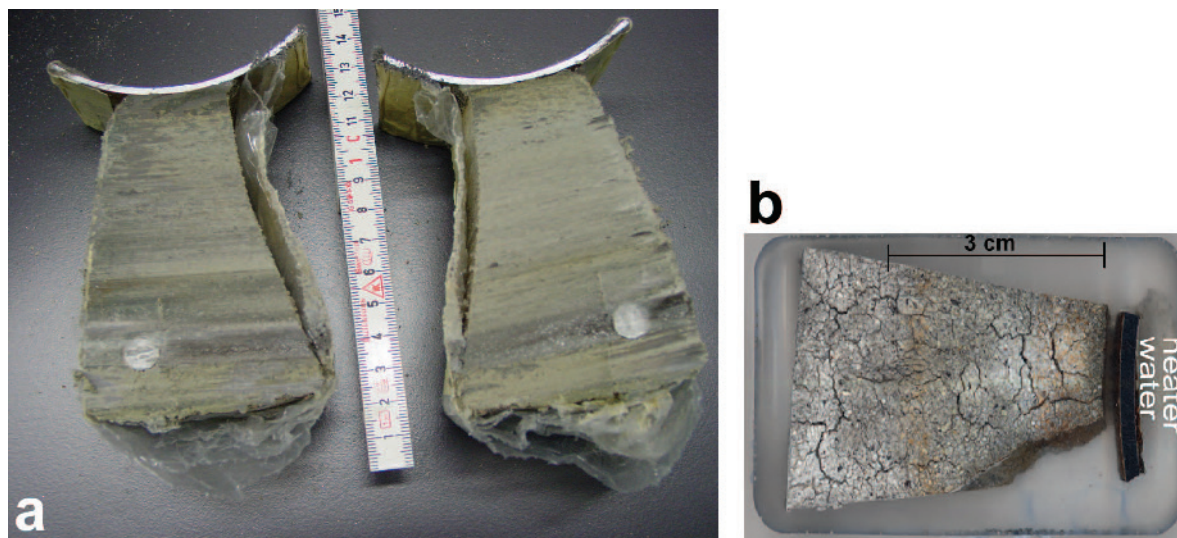

Figure 2. (a) Preparation of the clay sample with the steel contact. (b) Sample after freeze drying, resin impregnation, and polishing, as used for SEM and μ-Raman analysis.

resolution (1024 × 800 pixels), but shorter dwell time, was used to acquire backscattered electron (BE) images, which depict the average proton number at the beam location. The brightness and contrast of the maps were adjusted to reveal visible differences in gray values of important phases, often resulting in over- or undersaturation of phases of no interest. The EDX measurements were acquired for 60 s live time on spots or small homogenous areas, and analyzed semi-quantitatively without standardization using the EDAX Genesis software (Carl Zeiss Microscopy GmbH, Jena, Germany) with ZAF matrix correction. The data resulting in chemical profiles across the entire sample were acquired on a grid of 5 × 26 measurements, each scanning 1.52 mm × 1.19 mm for 3.13 min. The data for each of the five areas parallel to the steel interface were averaged; their range indicates the error of the method, assuming homogenous chemistry parallel to the interface. All detected elements heavier than fluorine were normalized to 100 wt.%, in contrast to methods with standards resulting in absolute compositions (*e.g.* electron microprobe). Errors in single EDX measurements were <2 wt.% in low-vacuum mode. In some measurements, oxygen was also quantified; much larger errors are expected in these cases.

μ-*Raman spectroscopy.* Raman spectroscopy was performed using a Jobin Yvon LabRAMHR800 (Horiba Jobin Yvon, Paris-Saclay, France) instrument, consisting of an Olympus BX41 confocal microscope (Olympus Corporation, Tokyo, Japan) coupled to an 800 mm focal-length spectrograph. An unattenuated He-Ne laser (20 mW, polarized 500:1) with an excitation wavelength of 632.817 nm (red) was focused on the sample surface and the Raman signal was collected in reflection mode. The sampled volume was a few μm^3 using a 100 × objective. Acquisition times were 2 × 10 s and 2 × 120 s for iron phases and clay matrices, respectively. The spectra were recorded with the *Labspec* V4.14 software (Horiba Jobin Yvon, Paris-Saclay, France). Fluorescence caused an enormous background in spectra from the clay matrix, possibly as an artefact of the natural organic matter present in bentonite.

RESULTS

Petrophysical data for the clay

Data measured as a function of the radial distance from the steel ring located in the center of the cage include water contents and wet densities (Table 1). Profiles were located in the middle of block 3, as well as close to the interfaces with neighboring blocks above and below. Porosities, which were calculated from water contents and wet densities (see the Methods section), were found to be ~50 vol.%, but showed a slight decrease toward to the heater (at a distance of 0−1.5 cm) to ~48 vol.%. All samples were found to be fully saturated. The results indicate effective homogenization of the pellets during saturation and swelling.

XRD and XRF data

XRF. The chemical composition determined from XRF analyses at different distances from the Fe source were analyzed (Table 2). The Fe content increases toward the metal contact, from a distance of ~10 mm. This is in

Table 2. XRF analyses of samples at different distances from the Fe metal.

Max. dist. from iron	Unit	C1/2	C3	C4	C5	C6	C7	C8	ref.
	mm	4.5	6.0	10.0	18.5	25.5	31.5	36.5	MX-80*
SiO_2	wt.%	59.85	61.81	62.53	62.28	61.42	63.76	61.16	59.58
TiO_2	wt.%	0.16	0.16	0.16	0.16	0.16	0.17	0.16	0.2
Al_2O_3	wt.%	19.02	19.65	19.69	19.74	19.49	20.12	19.33	18.90
Fe_2O_3	wt.%	6.21	4.71	4.41	4.36	4.39	4.41	4.28	3.91
MnO	wt.%	0.02	0.01	n.d.	0.01	0.01	0.01	0.02	0.02
MgO	wt.%	2.42	2.38	2.36	2.35	2.37	2.40	2.37	2.56
CaO	wt.%	1.47	1.23	1.37	1.42	1.26	1.20	1.23	1.39
Na_2O	wt.%	2.23	2.36	2.22	2.29	2.20	2.18	2.15	1.95
K_2O	wt.%	0.55	0.59	0.57	0.58	0.54	0.54	0.55	0.6
P_2O_5	wt.%	0.06	0.06	0.06	0.06	0.06	0.06	0.06	0.09
LOI	wt.%	5.63	5.44	5.57	5.64	5.68	5.72	5.89	10.5
SUM	wt.%	97.61	98.40	98.93	98.90	97.57	100.57	97.20	99.70
Si/Al	at%/at%	2.67	2.67	2.69	2.68	2.67	2.69	2.68	2.67
Fe/Si	at%/at%	0.08	0.06	0.05	0.05	0.05	0.05	0.05	0.05
Fe/Al	at%/at%	0.21	0.15	0.14	0.14	0.14	0.14	0.14	0.13
Mg/Al	at%/at%	0.16	0.15	0.15	0.15	0.15	0.15	0.16	0.17
Ca/Na	at%/at%	0.37	0.29	0.34	0.34	0.32	0.30	0.32	0.39

* Reference MX-80 material from the American Colloid Company (Svensson *et al.*, 2011)

agreement with finer-resolution EDX data presented below, which also indicate an increase in Fe in the first 10 mm. The other elements show no trend with distance. Note that the slightly lower Si and Al concentrations close to the metal contact are explained entirely by the larger Fe content in these samples. The samples C4−C6, unaffected by the Fe enrichment, display similar elemental composition to the reference MX-80 analyzed by Svensson *et al.* (2011) (Table 2). The slight difference in Fe content is due to the different loss on ignition (LOI) values. This is indicated by the very similar elemental Fe/Si and Fe/Al ratios.

The Ca/Na elemental ratios derived for seven XRF samples are in the range 0.29−0.37, slightly lower than the value of 0.39 determined for the reference MX-80 (Svensson *et al.*, 2011). This suggests a slight enrichment of Na^+ on the clay exchanger which might have occurred by equilibration with the Na-rich Kunigel bentonite block adjacent to the sampled MX-80 (Figure 1). Equilibration of exchangeable cations between the different bentonite materials in the ABM1 test has been shown by Dohrmann *et al.* (2013). On the other hand, the Ca/Na ratios derived for XRF samples are generally smaller than those derived from EDX analyses (see section below). The reason for this difference is not clear; it may be a result of imprecise EDX data for the Na present in low concentrations, leading to Ca/Na ratios which are too high.

XRD. The material scraped off the steel surface facing the clay was analyzed by XRD. All reflections in the pattern can be explained by the presence of gypsum, smectite, quartz, and numerous iron phases (Figure 3). The presence of anhydrite is indicated by a small peak at the position of the major anhydrite reflection. Strong reflections of lepidocrocite, siderite, goethite, and magnetite reveal the presence of both Fe^{2+} and Fe^{3+}. The XRD results are in agreement with μ-Raman data collected from the water-side of the metal (see section below), in which all these iron phases were also

identified, in addition to hematite. The presence of anhydrite and gypsum was also confirmed by the μ-Raman spectra (see section below).

The XRD patterns from the steel surface−clay were analyzed (Figure 4). Without specific clay preparation, investigation of the 001 reflection of smectite is inappropriate. In the present measurements, the peak position and form depend mainly on the hydration of the clay, which could not be controlled during sampling and measurement. The reflection at 62º is indicative of dioctahedral clays (060). The peak at 60º is assigned to quartz, but overlaps the position of a possible tri-octahedral 060 reflection (*e.g.* saponite or biotite). Most of the other phases interpreted from these patterns (quartz, cristobalite, gypsum, feldspars, mica) are known to be present in the MX-80 reference (Svensson *et al.*, 2011, NAGRA, 2011). Small reflections indicate the presence of goethite in C5 and of anhydrite in C9.

None of the reflections indexed shows a clear gradient across the profile. Other variations in peak heights are not systematic and can be explained by large grain sizes compared to sample volume and crystal-lographic preferred orientations of large grains. The cristobalite peak, however, is smaller in C1−C3 than in C4−C9, and gypsum is absent from C8 and C9.

Mineral chemistry of the corrosion layers

The metal−water side. The metal surface opposite the metal−clay interface (Figure 2b) was in contact with water circulating between central heater and the metal ring of the cage. The reason for studying this interface was to obtain insight into the corrosion process and compare the data with those obtained from the metal–clay side. Moreover, the identification of iron corrosion products by μ-Raman is more straightforward than on the opposite metal−clay side because the latter spectra were found to be affected by strong fluorescence. Raman spectra of the clay-free corrosion layer facilitated the subsequent Raman analysis of the contact area between the metal and the clay.
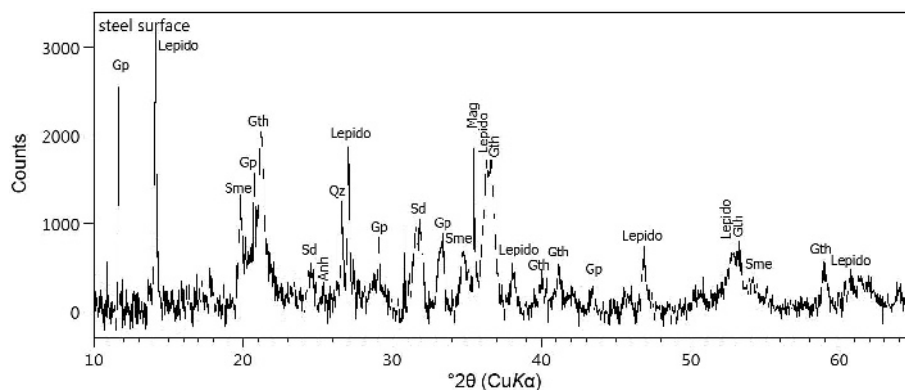

Figure 3. XRD pattern of the material scraped off the steel surface (Gp: gypsum, Lepido: lepidocrocite, Sme: smectite, Gth: goethite, Sd: siderite, Anh: anhydrite, Qz: quartz, Mag: magnetite; abbreviations after Whitney and Evans, 2010).
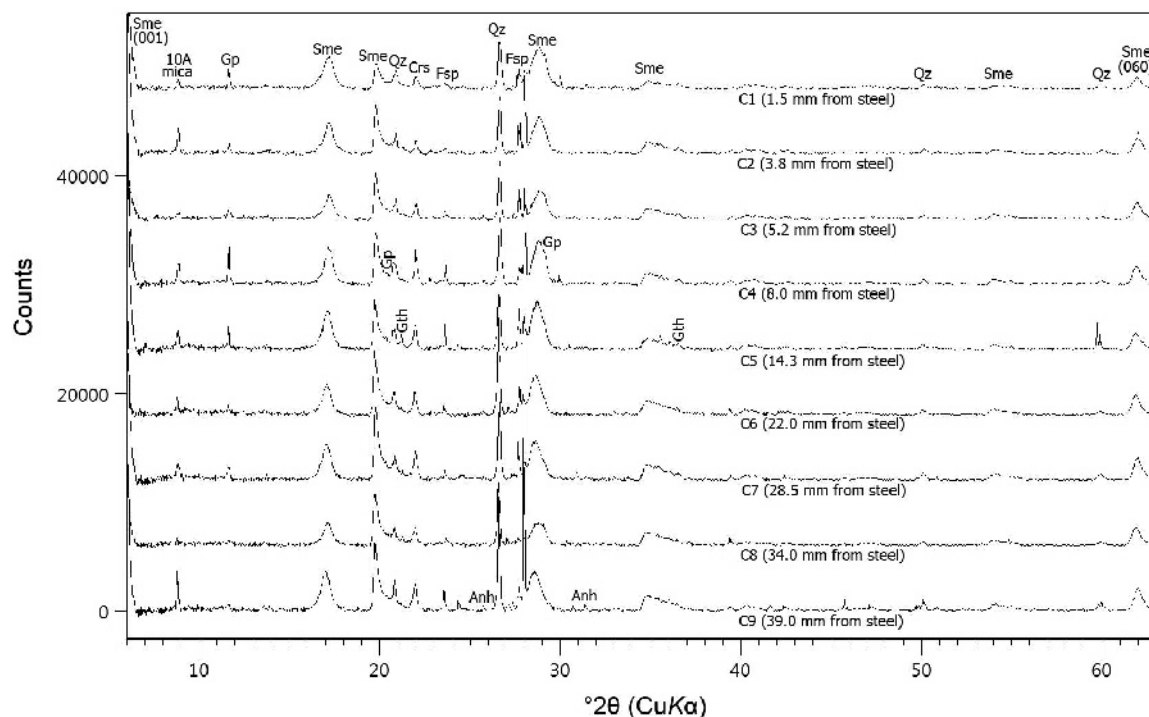
Figure 4. XRD patterns of the profile from the steel into the bentonite. The distances of the midpoints of sampled layers from the steel surface are indicated; counts are given for the lowest pattern C9. Consecutive patterns are shifted up by 6000 counts (Sme: smectite, Gp: gypsum, Qz: quartz, Crs: cristobalite, Fsp: feldspar, Anh: anhydrite, Gth: goethite).

The backscattered electron image of the metal−water contact area exhibits an irregularly shaped surface layer ~40−50 µm thick, with gradually increasing porosity (Figure 5). The patchy texture next to the bright metal surface is caused by different shades of variably sized grains. Adjacent to the interface, there is an aggregation of lighter-gray material of variable thickness (<5−20 µm) (Figure 5, lower right). Further away,
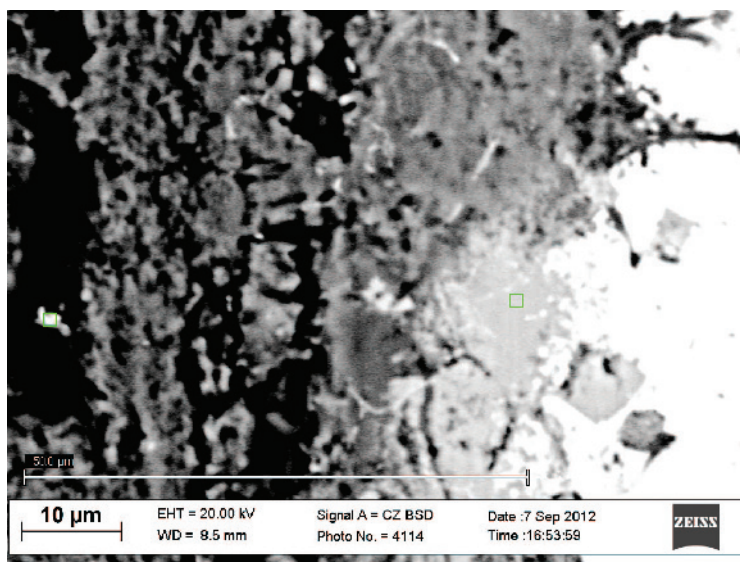
Figure 5. BSE-SEM image of a section across the metal and its corrosion layer facing the waterside; the metal surface is visible as a white area on right side − it has irregular contact with the corrosion layer to the left. The green square close to the metal represents the measurement area of the Raman spectrum corresponding to Figure 6a, green square further away from metal represents the measurement area of the Raman spectrum corresponding to Figure 6b.
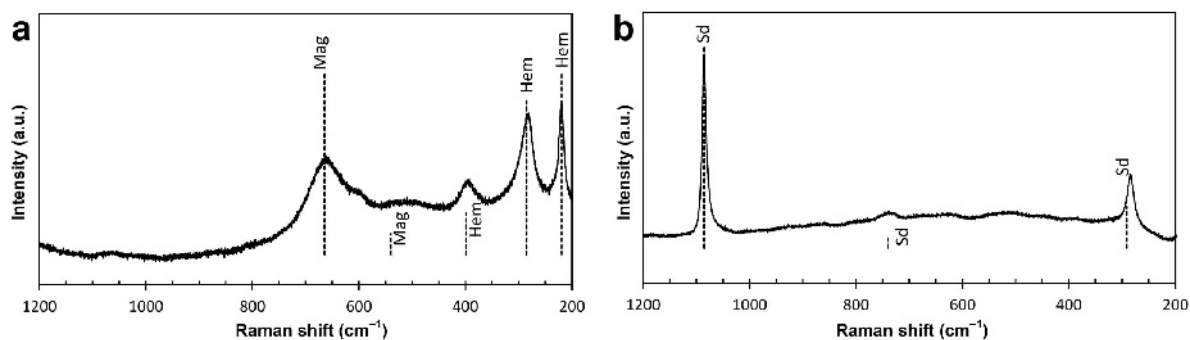
Figure 6. Selected Raman spectra of corrosion products obtained at the metal−water side of the corrosion layer: (a) spectrum taken 5 μm from the metal contact; (b) spectrum taken 50 μm from the metal contact. The dashed lines show reference-band positions and relative heights − Mag: magnetite, Hem: hematite, Sd: siderite (abbreviations after Whitney and Evans, 2010).

darker and more porous material dominates which is interspersed with brighter aggregates.

The different gray values of these materials reflect their different chemical composition (mean atomic number), which is dominated by Fe and O as indicated by semi-quantitative EDX analysis. The brighter material (Figure 5) was found to have a distinctly higher atomic Fe/O ratio than the darker one (data not shown). Trace amounts of Si and S were also detected. This indicates different Fe corrosion products, which was confirmed by μ-Raman spectroscopy. The light gray material close to the Fe surface (Figure 5) was found to consist of magnetite and, to a minor extent, hematite (Figure 6a, marked with a green square in Figure 5). Further away from the iron source, siderite was identified as the main Fe phase (Figure 6b). Some goethite and lepidocrocite (spectra not shown) were also observed. Siderite could also be identified by comple-

mentary SEM/EDX analysis. Well crystallized siderite grains were formed towards the outer contact of the corrosion layer (see bright grains at the right of Figure 5 marked with a green square).

The metal−clay side. The metal surface layer facing the clay has a different texture and denser habit (Figure 7): aggregates of bright and dark particles (diameter ~5−30 μm) form an irregular mesh. Chemically, the material was found to be composed of the elements Fe, Si, Al, Ca, Mg, and Na (besides O and C) with variable S contents as indicated by EDX spot analyses. The Fe contents revealed important variations with distance from the metal surface (Figure 8a), which are visible in backscattered electron images as variations in the brightness of the particles, with greater amounts of Fe associated with brighter particles. The Fe and Si profiles (shown as elemental ratios) from spot analyses indicate
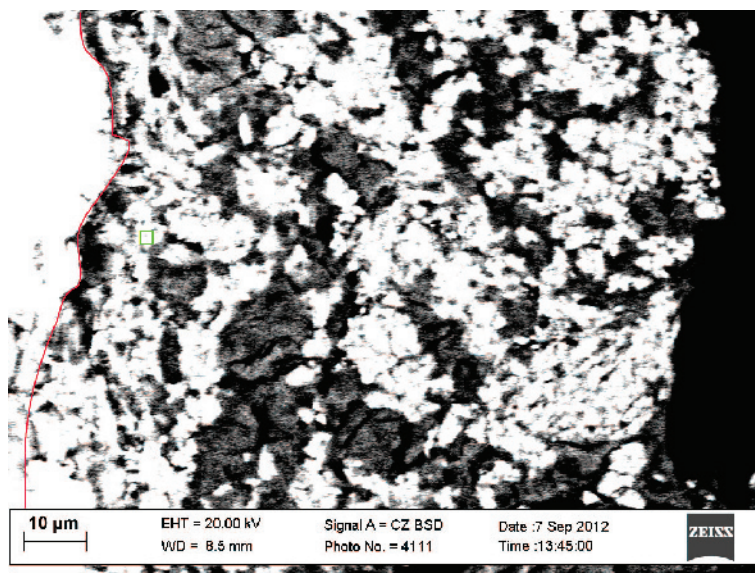

Figure 7. BSE-SEM image of a section across the metal and corrosion layer facing the clay. The red line delineates the contact between the metal and the corrosion layer. The black area on the right corresponds to a resin-filled gap between the metal and the clay formed during freeze drying. The green square represents the measurement area of the Raman spectrum shown in Figure 9.
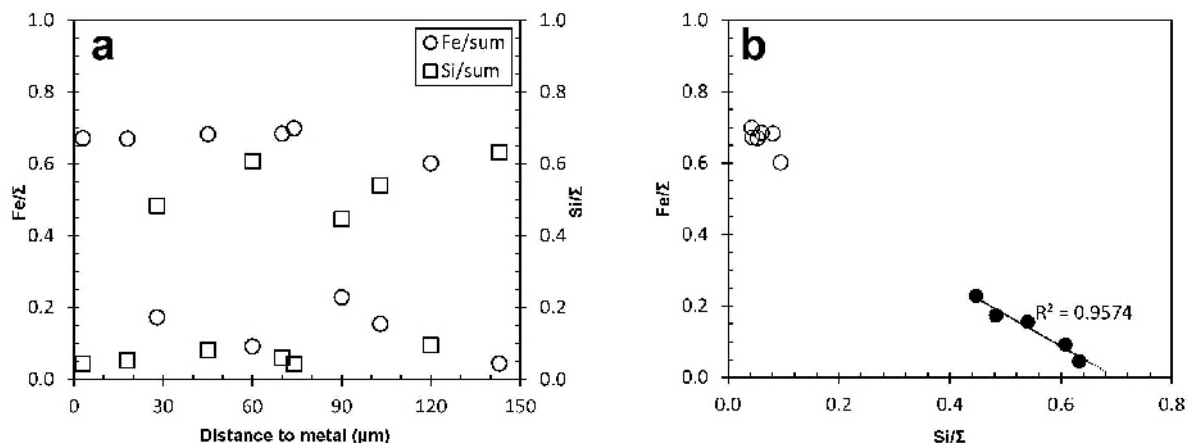
Figure 8. (a) Fe and Si *vs.* distance to metal in the corrosion layer (shown as atomic ratios Fe/(Si+Al+Mg+Na+K+Fe+S+Cl) (or Fe/Σ) and Si/(Si+Al+Mg+Na+K+Fe+S+Cl) (or Si/Σ). (b) Fe/Σ *vs.* Si/Σ. Open symbols: spots with high Fe/Si, closed symbols: spots with low Fe/Si.

two distinct groups of grains or grain aggregates: one with high Fe and low Si (bright grains) and one with low Fe and high Si (dark grains). The Fe and Si contents for the latter group are anti-correlated (Figure 8b) and this trend extends further into the Fe-enriched clay (data not shown).

Analysis by μ-Raman spectroscopy turned out to be more challenging on the clay side because of strong fluorescence radiation and fuzzier spectra. Nevertheless, siderite and, to a lesser extent, magnetite could be identified in the light gray particles (green square marked in Figure 7 corresponds to the Raman spectrum in Figure 9). The large fluorescence acquired from the dark gray particles indicates the presence of a clay matrix.

Mineral chemistry in the clay beyond the corrosion layer

Elemental mapping and phase identification. Imaging by SEM revealed the dense homogeneous texture of the clay and confirmed the macroscopic observation that the original granular texture had been destroyed during the course of the *in situ* experiment. Note that the cracks

observed (Figures 2b, 10) were formed during drying of the SEM sample. The elemental composition of the clay close to the metal contact but beyond the corrosion layer was analyzed by BSE-SEM imaging and qualitative elemental EDX maps (Figure 10). The black rim on the right hand side of each image represents the gap (induced by sample preparation) between the metal (including the corrosion layer) and the clay. The mapping thus covers the first 4 mm from the contact. Close to the contact, the concomitant enrichment of Ca and S points to the presence of anhydrite or gypsum. μ-Raman analysis of the same area indicates anhydrite as predominant and gypsum as a secondary phase (data not shown). For Si and Al, no trend with distance from the iron source was observed within the first 4 mm (Figure 10) and also beyond this distance as detailed below. The bright spots (~10−50 μm in size) noted on the Si map are probably SiO_2 particles. For Mg also, no trend is visible in the mapping, but a slight trend was noted from the quantitative area measurements (see below).
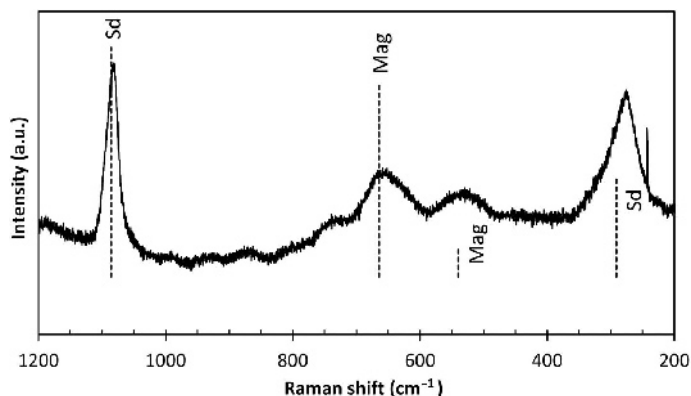

Figure 9. Selected μ-Raman spectrum in the 100 μm layer contacting the Fe surface. The dashed lines refer to the main reference-band positions and relative heights of siderite (Sd) and magnetite (Mag).
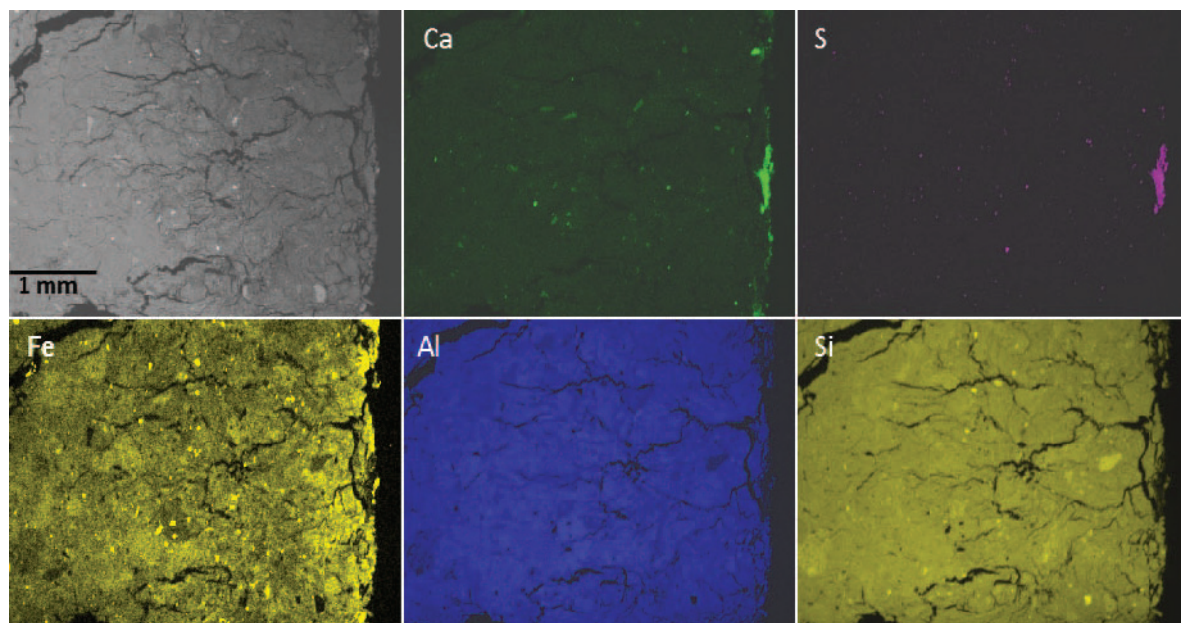
Figure 10. BSE-SEM image (top left) and EDX element maps of the clay sample close to the metal contact. Light colors represent high, dark colors low elemental concentrations. The contact gap/clay is on right hand side (see text). For Fe, higher concentrations are visible in the first 1 mm, next to the gap/clay contact.

Iron is also enriched in the clay matrix within the first 1 mm (right hand side of Figure 10). Due to the surface preparation and microscopic method chosen, this matrix appears to be structurally and chemically homogeneous and cannot be resolved further, *e.g.* it is possible that neo-formed iron phases cannot be localized. Adjacent to the gap, Fe-rich particles are observed (Figure 10). Most of the particles were found to be siderite as indicated by Ca levels which had concomitant increases, and are therefore considered to be part of the corrosion layer described above. Fe-rich particles further away from that gap are interpreted as pre-existing; according to quantitative image analysis they occupy only 0.4% of the area. Some of these particles were found to be enriched in sulfur, suggesting pyrite. A few bright particles in the Fe map are enriched in K, Si, and Al (but not in S), which might represent illite, present as an accessory mineral in the original MX-80 material (see the Methods section). Others, which are more abundant at the gap/clay contact, show no enrichment in K, but contain some Si, Al, Ca, and Mg (data not shown). Because of their small size it was not possible to identify the mineralogy of these particles.

Quantitative EDX profiles. The relationships between the elements were further studied by quantitative area measurements (see the Methods section). These were conducted on a fairly large area of 39.5 mm $\times$ 5.9 mm facing the metal contact. The total area was divided into five rows and 26 columns, thus corresponding to 130 cells. Each cell corresponds to one EDX area measurement. Averaged EDX analyses of five individual measurements (referred to as 'area measurements' below) were calculated for each column. Another run involved manually selected EDX spot measurements of the clay matrix avoiding any visible grains (referred to as 'spot measurements'). The spot measurements were performed within a region of 40 mm $\times$ 0.45 mm. The Fe profile, expressed as Fe/Al ratio, depicts a distinct decrease as a function of distance from the Fe metal surface within the first ~10 mm (Figure 11a). Zooming close to the Fe contact (Figure 11b, note logarithmic scale) and including the spot analyses in the corrosion layer, the strong enrichment is observed to be limited to ~150 μm from the Fe contact. In this zone, a steep Fe drop is indicated, which is followed further out by a much flatter Fe decrease. Furthermore, the profile also suggests slightly greater Fe/Al levels in the area 10−22 mm from the Fe contact but this increase relative to the clay further away is almost within the range (calculated from five measurements of different areas at identical distances from the metal). The fairly small range of the area samples (Figure 11a) indicates a small lateral variation in Fe (and also in the other elements), indicating homogeneous chemical composition in the clay matrix. The data thus suggest that the random error is small, although the systematic error in EDX data may be large (up to 2 wt.% absolute, see the Methods section). The Fe/Al ratios of the clay matrix beyond 21 mm obtained by EDX are 0.11−0.12, slightly smaller than the Fe/Al ratio (0.14) obtained by XRF bulk analysis of the same clay material (Table 2, see section
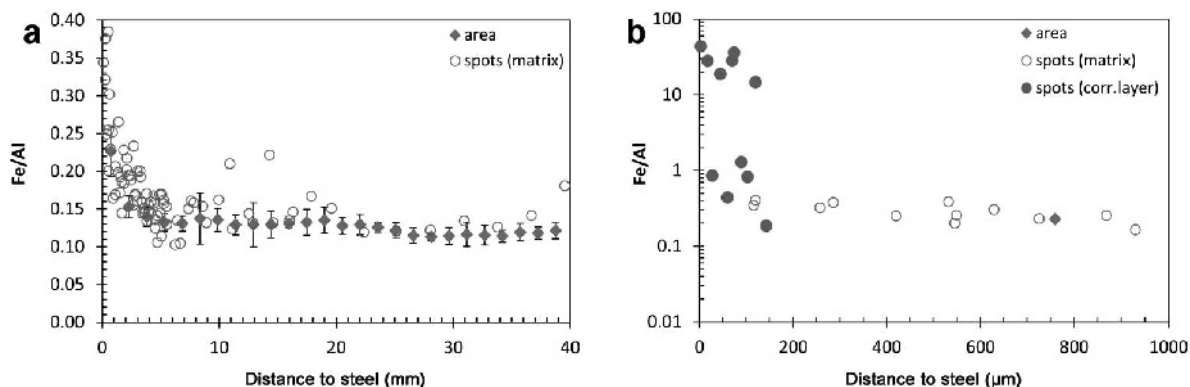
Figure 11. Fe/Al atomic ratio (EDX) as function of distance to the Fe source: (a) area and spot measurements; bars represent the range of five measurements with identical distance to steel; (b) area and spot measurements (in clay matrix as well as corrosion layer) within the first mm.

below). This difference is explained by the systematic error in the EDX measurements.

Image analysis was performed on the Fe maps in order to evaluate whether the Fe enrichment is primarily due to separate Fe particles or not. Relative Fe intensities (gray values) of a total area map of 5.9 mm × 39.5 mm (excluding the corrosion layer) were compared to that in which Fe-rich particles were subtracted by image analysis. The resulting intensities as a function of distance (Figure 12) reveal no significant difference between the total area and the matrix only. This indicates that the Fe enrichment occurs primarily in the clay matrix and is not caused by an enrichment of Fe-rich particles, which make up only 0.4% of the surface (see above). The large scattering in Fe intensities is caused by the very thin stripe analyzed, as well as by an unstable electron beam during the long mapping acquisition.

The main elements of the clay, namely Si and Al, do not exhibit any trend with decreasing distance to the metal surface. The Si/Al ratios of the area measurements

as function of distance from the metal contact were found to remain remarkably constant (2.52−2.54) (Figure 13a). The range of the area measurements is small (within the symbols in Figure 13a), suggesting a low random error. The Si/Al ratio obtained from XRF bulk analysis (Table 2) is somewhat higher (2.67−2.69), again suggesting a systematic error in the EDX measurements. The spot analyses from the corrosion layer display more variable Si/Al ratios, but neither a decrease nor an increase relative to the "background" value was observed (Figure 11b).

The Mg profile, expressed as a Mg/Al ratio, calculated from the area measurements, was generally found to display a narrow range of values (~0.15), which corresponds to that obtained from XRF bulk analyses (Table 2). Close to the contact, however, there is a slight increase (Figure 14a). The ratios for the matrix data plot slightly above the area data. The single-spot values in the corrosion layer display two groups (Figure 14b): the first one with only a slight increase in Mg/Al ratio and high Si (*cf.* section on corrosion layer); the second one
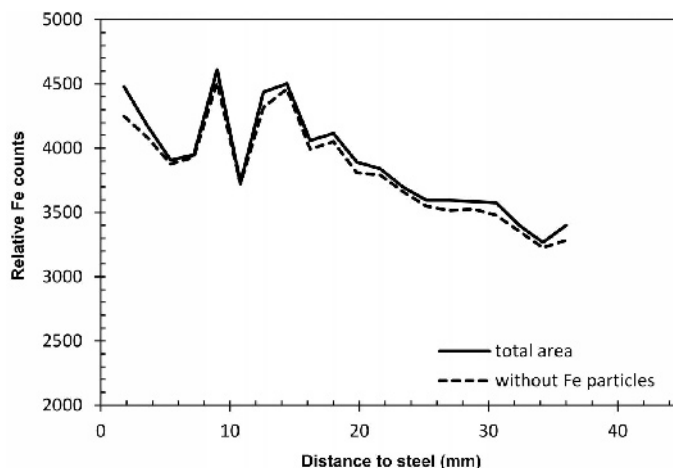

Figure 12. Relative Fe counts obtained by image analysis as a function of distance from the Fe source shown for total area and total area with Fe particles subtracted.
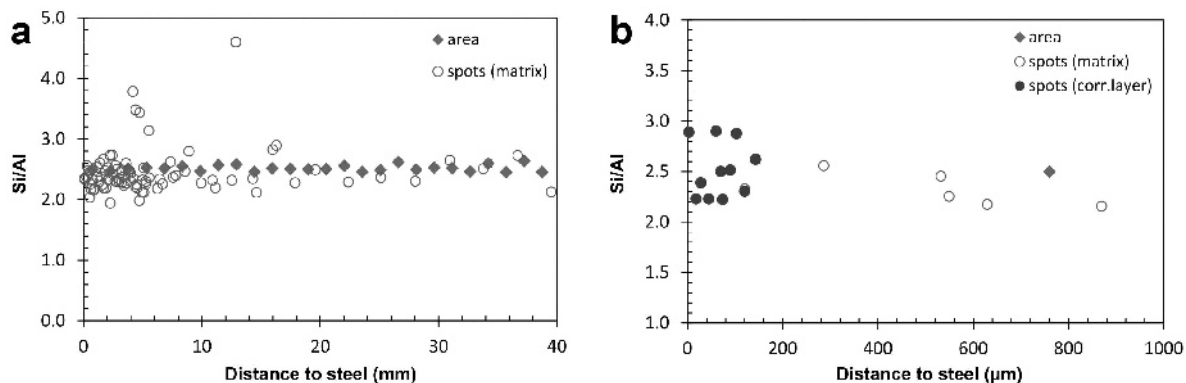
Figure 13. Si/Al atomic ratio as a function of the contact with the Fe source: (a) area and spot measurements; (b) area and spot measurements (in the clay matrix as well as in the corrosion layer) within the first mm. The range of area measurements (five measurements with identical distance from metal) is less than the size represented by the symbols.

with significantly higher Mg/Al ratios and low Si. Siderite, a prominent constituent of the corrosion layer (see above), may incorporate Mg (and Ca) in its lattice. This is probably the main reason for the observed large Mg/Al values compared to the bulk clay. The slightly higher Mg/Al ratios noted for the first group of spot measurements, which contains more Si, Al, and lower Fe contents (*cf.* section on corrosion layer), are similar to the ratios in the matrix close to the contact (see the Discussion section below).

Ca/Na elemental ratios of the total area analyses show important variations between 0.39 and 0.70, but no trend with regard to distance from the metal source (data not shown). The large variation is interpreted as a consequence of the inhomogeneous distribution of calcite and anhydrite particles in the clay in the contact area.

DISCUSSION

Quantification of the Fe-transfer process

The amount of Fe transferred to the clay can be estimated roughly from EDX analysis of Fe profiles. The Fe is concentrated in a layer ~10 mm thick (Figure 15).

The data also hint at a slight Fe enrichment at a distance of $10-22$ mm, but this is close to the range of analytical uncertainty (see the Results section). The background Fe concentration in the clay, $[Fe]_{c,\text{true}}$ (wt.% and g/kg dry clay), is derived from the averaged XRF analyses of the clay not affected by the Fe enrichment front (Table 2). First, the Fe concentrations from (semi)-quantitative EDX data need to be calibrated. This is done by averaging the EDX analyses from the samples located at $25-39$ mm from the contact which yields $[Fe]_c$. This apparent background Fe is related to the "true" background Fe by the calibration factor f_c where $[Fe]_{c,\text{true}} = f_c \times [Fe]_c$. The total increase in Fe, ΔM_{Fe}, is obtained by accounting for the cylindrical geometry of the Fe source (Figure 15) and the dry density, ρ_b, of the clay:

$$\Delta M_{\text{Fe}} = \sum_{n=1}^{z} (r_n^2 - r_{n-1}^2)\pi h \rho_b f_c (|Fe|_n - |Fe|_c) \qquad (1)$$

where n is the area number corresponding to the measured Fe concentration $[Fe]_n$ and r_n is the radius of the circle including the radius of the Fe source (r_o) and the distance from the source to the area n; z is the
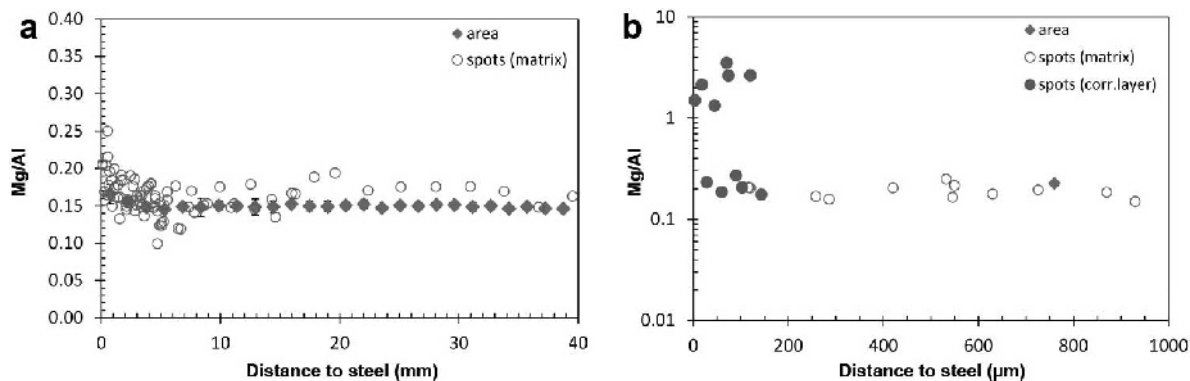

Figure 14. Mg/Al atomic ratio as function of the contact with the Fe source: (a) area and spot measurements; bars represent the range of five measurements with identical distance to steel; (b) area and spot measurements (in the clay matrix as well as in the corrosion layer) within the first mm.
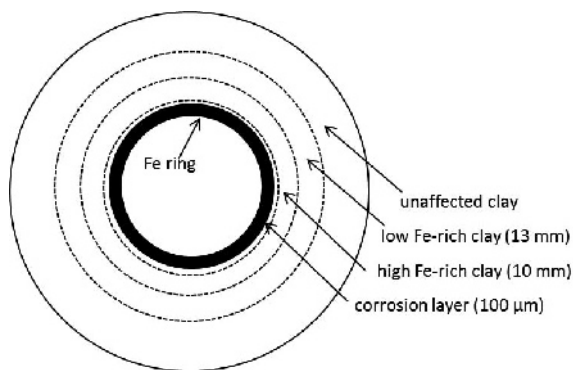
Figure 15. Top view of the inner metal ring of the cage surrounded by the corrosion layer and the Fe-enriched clay layer (not to scale, see text).

number of areas in which Fe is increased. The parameter h is the unit height of the cylinder, taken to be 10 mm.

The amount of Fe transferred to the clay can be converted to the average corrosion depth d_{corr} of the Fe source:

$$d_{corr} = \frac{\Delta M_{Fe}}{\rho_{Fe}} \frac{1}{A_s} \qquad (2)$$

where ρ_{Fe} is the density of Fe metal and A_s is the unit surface of the Fe source, equal to $2r_o\pi h$.

In order to estimate a lower and upper range of d_{corr}, two cases (with the parameter values shown in Table 3) were considered.

In the first case, it was assumed that the Fe increase in the clay is limited to the area of ~10 mm and that only 50% of the Fe in the 100 μm thick corrosion layer stems from the corrosion process, the remaining 50% being attributed to the initial corrosion layer before the start of the experiment. The latter assumption is arbitrary as it is not known what the average thickness of the corrosion layer at the start of the experiment was. The calculation yields a corrosion depth of 22.2 μm. Considering a test duration of ~800 days, an average corrosion rate (CR) of ~10 μm/y was deduced.

In the second case, the Fe increase in the clay was assumed to extend to an area distance of 22 mm and that all of the Fe in the corrosion layer stems from the corrosion process. This yields a corrosion depth of 35.3 μm and a corresponding average CR of ~16 μm/y.

The above estimates are associated with considerable uncertainties, but the corrosion rates obtained are not unreasonable. They reflect variable redox and saturation conditions in the corrosion history with residual O_2 occurring in the partially saturated pores of the clay and in the gaps. Upon O_2 consumption by corrosion reactions, conditions changed and became reducing for the remainder of the test period. This process is expected to lead to a significant decrease in the corrosion rates with time (*e.g.* King, 2008). Applying the semi-empirical relationships for a mean CR (mm/y) as a function of temperature (°K) from Foct and Gras (2003):

$$CR = 1.042 \times e^{-1340/T} \text{ (aerobic conditions)} \qquad (3)$$

$$CR = 0.364 \times e^{-1300/T} \text{ (anaerobic conditions} \\ \text{for corrosion times of } 0.5-15 \text{ y)} \qquad (4)$$

one obtains, for an average temperature of 100°C, 29 μm/y and 11 μm/y for aerobic and anaerobic conditions, respectively. The estimated CR values derived above are closer to the anaerobic rate obtained from equation 4.

As a further exercise, an average apparent diffusion coefficient (D_a) for Fe(II) can be estimated from the relationship:

$$x \approx 2\sqrt{D_a t} \qquad (5)$$

where x is the mean diffusion distance that a species will have diffused in time t, taken to be 5 mm, and t is the diffusion time, taken to be 800 days. This yields a diffusion coefficient D_a of 9×10^{-14} m²/s. The calculation implicitly assumes near-saturated conditions, required for Fe^{2+} diffusion to take place. The saturation history in block 3 is not known. Assuming that conditions around the Fe source were saturated for half of the test period only (400 days) and that diffusion under unsaturated conditions is slow compared to saturated ones, then application of the above equation yields a value for $D_a = 1.8 \times 10^{-13}$ m²/s.

The estimated D_a values are supported by a laboratory study on Fe^{2+} diffusion through bentonite by Xia *et al.* (2005) who evaluated the Fe profile in the

Table 3. Parameters used to estimate corrosion depth (see text).

Parameter	Description	Value	Comment
r_0	Radius of the iron ring	62.0 mm	
ρ_b	Bentonite dry density	1.44 g/cm³	See Table1
$[Fe]_{b,true}$	'true' background Fe	30.5 g/kg$_{clay}$	Av. conc. of samples C6−C8 from XRF analyses (Table2)
$[Fe]_b$	Measured background Fe	25.1 g/kg$_{clay}$	Av. conc. of EDX area meas., 25−39 mm from Fe contact
H	Height of the cylinder	10 mm	
ρ_{Fe}	Fe density	7.874 g/cm³	

clay by proposing a fast and slow diffusion process, with $D_a \approx 10^{-12}$ m^2/s and $\approx 10^{-14}$ m^2/s, respectively. D_a values for Ni^{2+}, another divalent transition element, for compacted bentonite were found to be ~5×10^{-12} m^2/s (compilation of Yu and Neretnieks, 1997), which is distinctly greater than the values obtained for Fe^{2+} by Xia *et al.* (2005). For diffusion of Co^{2+} in compacted bentonite, Molera and Eriksen (1998) determined D_a values in the range $1-2 \times 10^{-13}$ m^2/s , which is similar to the values for Fe^{2+} estimated here.

Fe—clay interaction and mineral alteration

The Fe phases formed by corrosion of the steel on the other side of the interface with the clay, as identified by Raman spectroscopy, were found to be magnetite, siderite, and, to lesser extent, hematite and Fe(III) oxyhydroxides (goethite and lepidocrocite). This indicates that the sample experienced both reducing and oxidizing conditions, assuming the sample did not experience oxidation during preparation/analysis (see discussion below).

The redox conditions in the test were initially oxidizing with residual air in the unsaturated bentonite material, the inner gap between the steel tube and the cage, and the outer gap between the cage and the rock. As indicated by the presence of siderite and magnetite, conditions switched to reducing, presumably due to the reaction of molecular O$_2$ with the Fe metal and Fe(II) minerals (*e.g.* pyrite) in the clay (*e.g.* Wersin *et al.*, 1994). After termination of the test, caution was taken during sampling to minimize contamination by O$_2$. No rigorous measures were taken, however, during sample preparation for EDX and Raman analyses. Thus, the presence of Fe(III) oxyhydroxides may either reflect conditions during the test or O$_2$ contamination during sample preparation and/or during Raman spectroscopy measurements. On the clay side, both siderite and magnetite as were identified dominant phases in addition to goethite and lepidocrocite close to the contact of the Fe source (100–150 μm). This finding indicates that reduced Fe(II) was at least partly preserved in the sample analyzed by SEM and μ-Raman spectroscopy.

The nature of the Fe phase in the iron-enriched clay matrix could not be identified, but this does not mean that other phases, such as Fe(III) oxyhydroxides or green rusts, did not form. As outlined in the Results section, Fe phases were more difficult to resolve in the clay by μ-Raman spectroscopy. Adjacent to the ~100 μm thick corrosion layer, which consists of a wedge-shaped structure of iron-rich and iron-poor aggregates, only newly formed siderite could be identified. In the Fe-enriched clay, however, most of the Fe is located in the matrix and not in separate particles, as indicated by image analysis. The form in which this Fe occurs is not clear. Various possibilities exist, including: (1) Fe oxyhydroxides (including green rusts); (2) Fe silicates; (3) Fe sorbed to the clay minerals; and (4) incorporation in the octahedral sheet of the clay, are discussed below.

(1) The presence of fine-grained Fe oxyhydroxide precipitates in the clay matrix is a viable possibility. This could be green rust of mixed Fe(II/III) oxidation state (*e.g.* fougerite) or some Fe(III) oxyhydroxide, such as lepidocrocite or ferrihydrite. Poorly crystallized or amorphous Fe oxyhydroxide would not be identified by XRD (Svensson and Hansen, 2013), but was observed using focused ion beam nanotomography combined with transmission electron microscopy (Lukas M. Keller, pers. comm.).

(2) The presence of newly formed Fe silicates, such as Fe serpentines (*e.g.* berthierine, cronstedite) or chlorite (*e.g.* chamosite) is not deemed to be likely. Such phases have not been identified in this study or in previous studies based on the ABM1 test (Kaufhold *et al.*, 2013; Svensson and Hansen, 2013). The characteristic 7 Å (~12.5º2θ Cu$K\alpha$) basal reflection of such non-swelling clays was not observed in any XRD pattern (Figure 4) and have not, to the present authors' knowledge, been identified in other experiments with compacted bentonite in contact with iron under repository-type settings (*e.g.* Carlson *et al.*, 2007).

(3) Fe(II) may be sorbed to the clay, either to interlayer sites by cation exchange reactions, or to edge surface sites by surface complexation (Tournassat, 2003). To evaluate the importance of sorbed Fe(II), it is useful to compare the amounts of measured Fe with the CEC of the clay. The maximum Fe content above the background in the clay observed is ~2 wt.% which corresponds to ~72 meq/100 g as Fe(II). This is close to the CEC (82 meq/100 g) for the reference MX-80 material (Svensson *et al.*, 2011). If all of the increase in Fe were to be sorbed to the clay it would make up almost all of the CEC. This would mean that the main exchangeable cation Na$^+$ would have been released into solution and moved diffusively along the Na gradient away from the metal. The Na and Na/Al profiles (not shown) indicate no decrease toward the metal contact, however. Sorbed Fe(II) cannot explain all of the measured Fe increase, therefore, but perhaps can account for a small fraction of it.

(4) Incorporation of Fe(II) into the octahedral sheets by substitution is not considered likely because of steric constraints. In fact, experimental data suggest a destabilization of the smectite structure upon reduction of Fe(III) to Fe(II) in the octahedral sheet (Lantenois *et al.*, 2005).

No indication of montmorillonite alteration in the (hot) Fe-clay contact zone from XRD data was found. The same finding was made in other bentonite samples in ABM1 in previous studies by Svensson and Hansen (2013) and Kaufhold *et al.* (2013). This is also supported by EDX analyses pointing to constant Si/Al ratios even in the corrosion layer. The only feature noted from EDX was the slight increase in Mg very close to the metal contact (<1 mm). This increase is not noted from XRF analyses, probably because of the coarser profile data.

The reason for the slight increase remains unclear, but it is interesting to note that a similar trend was observed for other bentonite materials in the ABM1 test (Kaufhold *et al.*, 2013) and also in a previous *in situ* experiment, termed LOT (Long-term Test of Buffer Material) (Karnland *et al.*, 2009). Moreover, an Mg increase in Febex bentonite close to a heating source was observed in a long-term laboratory test (Fernandez and Villar, 2010). Kaufhold *et al.* (2013) suggested tentatively the formation of Mg-rich trioctahedral domains in the clay based on FTIR spectroscopy. On the other hand, Svensson and Hansen (2013) suggested the neo-formation of separate trioctahedral clay phases (*e.g.* saponite).

The weakening of the XRD reflections for cristobalite close to the iron and heat source suggests that some SiO_2 dissolution occurred during the test. Similar XRD observations were made previously on other samples from the ABM1 test (Kaufhold *et al.*, 2013; Svensson and Hansen, 2013) and also in another similar *in situ* test termed TBT (Temperature Buffer Test) in which MX-80 blocks had been exposed to temperatures of up to 150ºC (Svensson and Hansen, 2013).

The increased temperature also induced precipitation of gypsum and anhydrite close to the heat source as shown by XRD and Raman data. Raman data indicate the predominance of anhydrite whereas XRD data indicate the predominance of gypsum. The reason for this difference may be related to the exposure of the XRD samples to air and moisture uptake during sample preparation. This may have induced conversion of anhydrite to gypsum. The presence of anhydrite close to the heat source in other bentonite samples of ABM1 was also found by Kaufhold *et al.* (2013) and the same observation was made in the *in situ* experiment LOT experiment (Karnland *et al.*, 2009).

CONCLUDING REMARKS

In the present microscopic study, a fully homogenized and saturated MX-80 pellet sample exposed to temperatures of up to 115ºC and artificial water for ~800 days close to an iron metal contact from the ABM1 test package was analyzed. The corrosion process led to the formation of a ~100 μm thick corrosion layer containing siderite, magnetite (identified by μ-Raman and XRD) as well as goethite and lepidocrocite (identified by XRD) associated with the montmorillonitic clay. On the rear side of the metal, which had been in direct contact with water during the test, hematite could also be identified. The formation of Fe(II) mineral phases demonstrates the reducing conditions in the *in situ* test. The presence of Fe(III) oxyhydroxides may either reflect the early oxic conditions in the test or be related to O_2 contamination during sample preparation and/or μ-Raman analysis.

Most of the Fe released by corrosion of metal infiltrated the first 10 mm of the clay. The Fe profiles from EDX analysis hint at a maximum distance of ~22 mm of increased Fe levels in the clay. From mass-balance considerations, Fe corrosion depleted an Fe metal layer of ~22−35 μm average thickness, which corresponds to an average corrosion rate of ~10−16 μm/y. In view of the variable redox conditions, the corrosion rate was also likely to be variable, albeit decreasing during the test. The estimated values are similar to those proposed for 'short-term' anaerobic iron corrosion rates at 100ºC, however, suggesting that test conditions were mostly anaerobic.

From the observed Fe enrichment front, an average apparent diffusivity for Fe^{2+} was also estimated to be in the range $1-2 \times 10^{-13}$ m²/s. This is similar to the Fe^{2+} diffusivities determined in Kunigel bentonite (Xia *et al.*, 2005).

The corrosion-derived Fe that diffused into the clay beyond the corrosion layer occurs predominantly in the clay matrix and not in discrete Fe particles. The nature of this Fe could not be identified. From the current data, fine-grained Fe oxyhydroxides, presumably in a mixed Fe(II/III) oxidation state, seem most likely. Sorbed Fe may constitute only a minor proportion of the total Fe transferred.

No indication of montmorillonite transformation or newly formed clay phases was found. Thus, no Fe-rich silicates, such as 1:1 clays, trioctahedral smectite, or newly-formed illite were observed. This finding confirms previous XRD results on different bentonite materials in the ABM1 tests. The EDX data indicate a slight increase in Mg in the clay close to the contact, confirming the result obtained by Kaufhold *et al.* (2013) and also data from the LOT experiment (Karnland *et al.*, 2009). The reason for this Mg increase close to the metal heater has not been resolved here. According to the work of Svensson and Hansen (2013) and Kaufhold *et al.* (2013) the enrichment may be related to the formation of trioctahedral smectites.

The stability of montmorillonite in contact with steel and exposed to rather elevated temperatures for ~2.5 y in a repository-like setting shown in these experiments is generally consistent with previous studies with similar settings (Karnland *et al.*, 2009; Fernandez and Villar, 2010; Kaufhold *et al.*, 2013; Svensson and Hansen, 2013).

Future analysis of the test packages ABM2 and ABM3, exposed to heat and Fe-bentonite interaction for longer time periods, will enable more conclusive statements on montmorillonite stability in repository settings. The study presented here is considered to represent a good basis for further investigations of Fe−bentonite interaction, notably on ABM samples exposed to corroding iron for longer periods of time.

ACKNOWLEDGMENTS

REFERENCES

Bradbury, M., Berner, U., Curti, E., Hummel, W., Kosakowski, G., and Thoenen, T. (2014) The long term geochemical evolution of the nearfield of the HLW repository. NAGRA Technical Report NTB 12-01, Wettingen, Switzerland. www.nagra.ch/en/downloadcentre.htm

Carlson, L., Karnland, O., Oversby, V.M., Rance, A.P., Smart, N.R., Snellman, M., Vähänen, M., and Werme, L.O. (2007) Experimental studies of the interactions between anaerobically corroding iron and bentonite. *Physics and Chemistry of the Earth*, **32**, 334–345.

Carrado, K.A. and Komadel, P. (2009) Acid activation of bentonites and polymer–clay nanocomposites. *Elements*, **5**, 111–116.

Charpentier, D., Devineau, K., Mosser Ruck, R., Cathelineau, M., and Villieras, F. (2006) Bentonite–iron interactions under alkaline condition: An experimental approach. *Applied Clay Science*, **32**, 1–13.

Christidis, G.E. and Huff, W.D. (2009) Geological aspects and genesis of bentonites. *Elements*, **5**, 93–98.

De Combarieu, G., Schlegel, M.L., Neff, D., Foy, E., Vantelon, D., Barboux, P., and Gin, S. (2011) Glass-iron-clay interactions in a radioactive waste geological disposal: An integrated laboratory-scale experiment. *Applied Geochemistry*, **26**, 65–79.

Didier, M., Leone, L., Greneche, J.-M., Giffaut, E., and Charlet, L. (2012) Adsorption of hydrogen gas and redox processes in clays. *Environmental Science and Technology*, **46**, 3574–3579.

Dohrmann, R., Olsson, S., Kaufhold, S., and Sellin, P. (2013) Mineralogical investigations of the first package of the alternative buffer material test. II. Exchangeable cation population rearrangement. *Clay Minerals*, **48**, 215–233.

Eisenhour, D.D. and Brown, R.K. (2009) Bentonite and its impact on modern life. *Elements*, **5**, 83–88.

Eng, A., Nilsson, U., and Svensson, D. (2007) Äspö Hard Rock Laboratory. Alternative Buffer Material. Installation report. SKB International Progress Report IPR-07-15, Stockholm, Sweden.
http://www.skb.com/publication/1633130/

Fernández, A.M. and Villar, M.V. (2010) Geochemical behaviour of a bentonite barrier in the laboratory after up to 8 years of heating and hydration. *Applied Geochemistry*, **25**, 809–824.

Foct, F. and Gras, J.-M. (2003) Semi-empirical model for carbon steel corrosion in long term geological nuclear waste disposal. Pp. 92–102 in: *Prediction of Long Term Corrosion Behaviour in Nuclear Waste Systems* (D. Ferron and D.D McDonald, editors). European Federation of Corrosion. ISBN 1902653874.

Gates, W.P., Bouazza, A., and Churchman, G.J. (2009) Bentonite clay keeps pollutants at bay. *Elements*, **5**, 105–110.

Gaudin, A., Gaboreau, S., Tinseau, E., Bartier, D., Petit, S., Grauby, O., Foct, F., and Beaufort, D. (2009) Mineralogical reactions in the Tournemire argillite after *in situ* interaction with steels. *Applied Clay Science*, **43**, 196–207.

Guillaume, D., Neaman, A., Cathelineau, M., Mosser-Ruck, R., Pfeiffert, C., Abdeloula, M., Dubessy, J., Villéras, F., Baronnet, A., and Michau, N. (2003) Experimental synthesis of chlorite from smectite at 300ºC in the presence of

metallic Fe. *Clay Minerals*, **38**, 281–302.

Guillaume, D., Neaman, A., Cathelineau, M., Mosser-Ruck, R., Peiffert, C., Abdelmoula, M., Dubessy, J., Villiéras, F., and Michau, N. (2004) Experimental study of the transformation of smectite at 80 and 300ºC in the presence of Fe oxides. *Clay Minerals*, **39**, 17–34.

Güven, N. (2009) Bentonites – clays for molecular engineering. *Elements*, **5**, 89–92.

Jodin-Caumon, M.-C., Mosser-Ruck, R., Rousset, D., Randi, A., Cathelineau, M., and Michau, N. (2010) Effect of a thermal gradient on iron-clay interactions. *Clays and Clay Minerals*, **58**, 667–681.

Jodin-Caumon, M.-C., Mosser-Ruck, R., Randi, A., Pierron, O., Cathelineau, M., and Michau, N. (2012) Mineralogical evolution of a claystone after reaction with iron under thermal gradient. *Clays and Clay Minerals*, **60**, 443–455.

Johnson, L., Marschall, P., Wersin, P., and Gribi, P. (2008) HMCBG processes related to the steel components in the KBS-3H disposal concept. SKB Report R-08-25, SKB, Stockholm, Sweden. 127 pp.
http://www.skb.com/publication/1857594/

Karnland, O., Olsson, S., and Nilsson, U. (2006) Mineralogy and sealing properties of various bentonites and smectite-rich clay materials. SKB Technical Report TR-06-30, Stockholm, Sweden.
http://www.skb.com/publication/1419144/

Karnland, O., Nilsson, U., Weber, H., and Wersin, P. (2008) Sealing ability of Wyoming bentonite pellets foreseen as buffer material – laboratory tests. *Physics and Chemistry of the Earth*, **33**, S472–S475.

Karnland, O., Olsson, S., Dueck, A., Birgersson, M., Nilsson, U., and Hernan-Hakansson, T. (2009) Long term test of buffer material at the Äspö Hard Rock Laboratory, LOT project. Final report on the A2 test parcel. SKB Technical Report TR-09-29, Stockholm, Sweden.
http://www.skb.com/publication/1961944/

Kaufhold, S., Dohrmann, R., Sanden, T., Sellin, P., and Svensson, D. (2013) Mineralogical investigations of the first package of the alternative buffer material test. I. Alteration of bentonites. *Clay Minerals*, **48**, 199–213.

King, F. (2008) Corrosion of carbon steel under anaerobic conditions in a repository for SF and HLW in Opalinus Clay. NAGRA Technical Report NTB 08-12, Wettingen, Switzerland.
www.nagra.ch/en/downloadcentre.htm

Kumpulainen, S., Carlsson, T., Muurinen, A., Kiviranta, L., Svensson, D., Sasamoto, H.,Yui, M., Wersin, P., and Rosch, D. (2010) Long-term alteration of bentonite in the presence of metallic iron. Posiva Working Report 2010-71, Olkiluoto, Finland and SKB Report R-10-52, Stockholm, Sweden.
http://www.skb.com/publication/2255832/

Lanson, B., Lantenois, S., Van Aken, P.A., Bauer, A., and Plançon, A. (2012) Experimental investigation of smectite interaction with metal iron at 80ºC: Structural characterization of newly formed Fe-rich phyllosilicates. *American Mineralogist*, **97**, 864–871.

Lantenois, S., Lanson, B., Mulller, F., Bauer, A., Jullien, M., and Plançon, A. (2005) Experimental study of smectite interaction with metal Fe at low temperature: 1. Smectite destabilization. *Clays and Clay Minerals*, **53**, 597–612.

Martin, F.A., Bataillon, C., and Schlegel, M.B. (2008) Corrosion of iron and low alloyed steel within a water saturated brick of clay under anaerobic deep geological disposal conditions: An integrated experiment. *Journal of Nuclear Materials*, **379**, 80–90.

Marty, N.C.M., Fritz, B., Clément, A., and Michau, N. (2010) Modelling the long term alteration of the bentonite barrier in an underground radioactive waste repository. *Applied Clay Science*, **47**, 82–90.

Meier, L.P. and Kahr, G. (1999) Determination of the cation exchange capacity (CEC) of clay minerals using the complexes of copper(II) ion with triethylenetetramine and tetraethylenepentamine. *Clays and Clay Minerals*, **47**, 386−388.

Molera, M. and Eriksen, T.E. (1998) Cation diffusion in compacted bentonite. *Mineralogical Magazine*, **62A**, 1007−1008.

Mosser-Ruck, R., Cathelineau, M., Guillaume, D., Charpentier, D., Rousset, D., Barres, O., and Michau, N. (2010) Effects of temperature, pH, and iron/clay and liquid/clay ratios on experimental conversion of dioctahedral smectite to berthierine, chlorite, vermiculite, or saponite. *Clays and Clay Minerals*, **58**, 280−291.

NAGRA (2002) Project Opalinus Clay: Safety report. Demonstration of disposal feasibility for spent fuel, vitrified high-level waste and long-lived intermediate-level waste (Entsorgungsnachweis). NAGRA Technical Report NTB 02-05, Wettingen, Switzerland. www.nagra.ch/en/downloadcentre.htm

NAGRA (2009) Performance of bentonite as buffer and sealing material: Status of R and D programme. NAGRA Arbeitsbericht NAB 09-12, Wettingen, Switzerland. www.nagra.ch/en/downloadcentre.htm

NAGRA (2011) Alternative Buffer Material − Status report. NAGRA Arbeitsbericht NAB 11-19, NAGRA, Wettingen, Switzerland. www.nagra.ch/en/downloadcentre.htm

Osacký́a, M., Šucha, V., Czímerová, A., and Madejová, J. (2010) Reaction of smectites with iron in a nitrogen atmosphere at 75ºC. *Applied Clay Science*, **50**, 237−244.

Papillon, F., Jullien, M., and Bataillon, C. (2001) Carbon steel behaviour in compacted clay: two long-term tests for corrosion prediction. Pp. 439−454 in: *Prediction of Long Term Corrosion, Behaviour in Nuclear Waste Systems*. (D. Feron and D.D. MacDonald, editors). European Federation of Corrosion Publications.

Perronnet, M., Jullien, M., Villieras, F., Raynal, J., Bonnin, D., and Bruno, G. (2008) Evidence of a critical content in Fe(0) on FoCa7 bentonite reactivity at 80ºC. *Applied Clay Science*, **38**, 187−202.

POSIVA (2013) Safety case for the disposal of spent nuclear fuel at Olkiluoto. Report Posiva 2012−14, Olkiluoto, Finland. www.posiva.fi/en/databank/posiva_reports#.VM4v0yxARrQ

Schlegel, M.L., Bataillon, C., Blanc, C., Prêt, D., and Foy, E. (2010) Anodic activation of iron corrosion in clay media under water-saturated conditions at 90 degrees C: characterization of the corrosion interface. *Environmental Science & Technology*, **44**, 1503−1508.

Schlegel, M.L., Bataillon, C., Brucker, F., Blanc, C., Prêt, D., Foy, E., and Chorro, M. (2014) Corrosion of metal iron in contact with anoxic clay at 90ºC: Characterization of the corrosion products after two years of interaction. *Applied Geochemistry*, **51**, 1−14.

SKB (2011) Long-term safety for the final repository for spent nuclear fuel at Forsmark. SKB Technical Report TR-11-01, Stockholm, Sweden. http://www.skb.com/publication/2345580/

Svensson, D., Dueck, A., Nilsson, U., Olsson, S., Sandén, T., Lydmark, S., Jägerwall, S., Pedersen, K., and Hansen, S. (2011) Alternative buffer material. Status of the ongoing laboratory investigation of reference materials and test package 1. SKB Technical Report TR-11-06, Stockholm, Sweden. http://www.skb.com/publication/2442994/

Svensson, D., and Hansen, S. (2013) Iron redox chemistry in two iron-bentonite field experiments at Äspö Hard Rock Laboratory, Sweden − studied by Fe K XANES and XRD. *Clays and Clay Minerals*, **61**, 566−579.

Tournassat, C. (2003) Cations−clays interactions: the Fe(II) case. Application to the problem of the French deep nuclear repository field concept. PhD thesis, University of Grenoble, France, 199 pp.

Wersin, P. and Birgersson, M. (2014) Reactive transport modelling of iron-bentonite interaction within the KBS-3H disposal concept: the Olkiluoto site as a case study. Pp. 237−250 in: *Clays in Natural and Engineered Barriers for Radioactive Waste Confinement* (S. Norris, J. Bruno, M. Cathelineau, P. Delage, C. Fairhurst, E.C. Gaucher, Höhn, E.H., A. Kalinichev, P. Lalieux, and P. Sellin, editors). Special Publications, **400**, Geological Society, London.

Wersin, P., Spahiu, K., and Bruno, J. (1994) Time evolution of dissolved oxygen and redox conditions in a HLW repository. SKB Technical Report TR 94-02, Stockholm, Sweden. http://www.skb.com/publication/9933/

Wersin, P., Johnson, L., and Schwyn, B. (2004) Assessment of redox conditions in the near field of nuclear waste repositories: Application to the Swiss high-level and intermediate level waste disposal concept. *MRS symposium proceedings*, **807** (V.M. Oversby and L.O. Werme, editors). Materials Research Society (MRS), Pittsburgh, Pennsylvania, pp. 539−544. (Scientific basis for nuclear waste management XXVII: Symposium held 15−19 June, 2003, Kalmar, Sweden.)

Wersin, P., Birgersson, M., Olsson, S., Karnland, O., and Snellman, M. (2007) Impact of corrosion-derived iron on the bentonite buffer within the KBS-3H disposal concept − the Olkiluoto site as case study. Posiva Report 2007-11, Olkilouto, Finland. www.posiva.fi/en/databank/posiva_reports#.VM4v0yxARrQ

Whitney, D.L. and Evans, B.W. (2010) Abbreviations for names of rock-forming minerals. *American Mineralogist*, **95**, 185−187.

Williams, L.B., Haydel, S.E., and Ferrell, R.E. Jr. (2009) Bentonite, bandaids, and Borborygmi. *Elements*, **5**, 99−104.

Wilson, J., Cressey, G., Cressey, B., Cuadros, J., Ragnarsdottir, K.V., Savage, D., and Shibata, M. (2006) The effect of iron on montmorillonite stability: (II) Experimental investigation. *Geochimica et Cosmochimica Acta*, **70**, 323−336.

Wollenberg, R. and Schröder, H. (2006) Herstellung und Charakterisierung von Bentonitsystemen für den Einsatz als Versiegelungsmaterial (Fabrication and characterization of bentonite systems for the use as sealing material). NAGRA Arbeitsbericht NAB 06-20, Wettingen, Switzerland.

Xia, X., Idemitsu, K., Arima, T., Inagaki, Y., Ishidera, T., Kurosawa, S., Iijima, K., and Sato, H. (2005) Corrosion of carbon steel in compacted bentonite and its effect on neptunium diffusion under reducing condition. *Applied Clay Science*, **28**, 89−100.

Yu, J.-W. and Neretnieks, I. (1997) Diffusion and sorption properties of radionuclides in compacted bentonite. SKB Technical Report TR 97-12, Stockholm, Sweden. http://www.skb.com/publication/13606/